Response of a turbulent separation bubble to zero-net-mass-flux jet perturbations

Wen Wu[*]

Department of Mechanical Engineering, University of Mississippi, Oxford, Mississippi 38677, USA

Charles Meneveau and Rajat Mittal

Department of Mechanical Engineering, Johns Hopkins University, Baltimore, Maryland 21218, USA

Alberto Padovan and Clarence W. Rowley

Department of Mechanical and Aerospace Engineering, Princeton University, Princeton, New Jersey 08544, USA

Louis Cattafesta[†]

Department of Mechanical Engineering, Florida State University, Tallahassee, Florida 32310, USA

The response of a turbulent separation bubble (TSB) to zero-net-mass-flux actuation is investigated via direct numerical simulations. Rectangular jets with their long axis oriented in the streamwise direction are used to generate unsteady streamwise vortices that mimic the streamwise elongated Görtler vortices found to be associated with the low-frequency unsteadiness of the TSB [Wu *et al.*, J. Fluid Mech., **883**, A45 (2019)]. Three sinusoidal actuation frequencies are investigated, corresponding to the two natural frequencies of the undistributed separation bubble (f_l and f_h with a ratio of $f_h/f_l = 2.5$) and a high frequency at $10 f_l$ motivated by a harmonic resolvent analysis. The results are compared to the baseline uncontrolled flow. Very-large scale (VLS), spanwise-rotating vortices are formed at f_l and f_h, causing a 50% reduction in the mean TSB length. A counter-rotating secondary vortex is induced locally by the VLS vortex in the f_l case and forms a vortex pair with the VLS vortex as they move downstream together. The interaction of the vortex pair facilitates their decay. The VLS vortex generated by the forcing at f_h is not strong enough to produce such a secondary vortex. Spectral analysis of the harmonic resolvent operator is used to quantify the receptivity of the flow to actuation at different frequencies. The perturbations that excite the most energetic response in the flow are indeed in the form of streamwise-elongated structures in the separation region at f_l and f_h. Energetic structures corresponding to the temporal mean obtained from the analysis are found to extend to distances far downstream of the separation bubble confirming the great sensitivity of the entire flow to such forcing.

---

[*]wu@olemiss.edu

[†]Present address: Department of Mechanical, Materials, and Aerospace Engineering, Illinois Institute of Technology, Chicago, Illinois 60616, USA.

I. INTRODUCTION

The separation of a boundary layer is most often detrimental to the aerodynamic performance of control surfaces. Flow control methods that eliminate or at least reduce the extent of separation can significantly improve system performance by increasing lift, or reducing drag and pressure losses. The literature on the subject of separation control is quite large. Numerous types of control techniques have been developed. For example, some techniques directly inject high streamwise momentum into the near-wall flow [1,2]. Others promote the transfer of higher momentum outer flow toward the wall to overcome the local adverse pressure gradient (APG) and prevent/delay separation [3,4]. Promoting the transition from laminar to turbulent flow by tripping devices or surface roughness, modifying the mean flow and its stability characteristics by large amplitude fluidic injection and suction, and inhibiting separation via streamwise vortices produced by vortex-generator-jet arrays are examples of the latter category. This study focuses on the role of control frequency in the effectiveness of this type of separation control.

Many recent studies have focused on separation with a laminar incoming flow [5–10]. There are a number of reasons to focus on laminar inflow. First, in a wide range of applications the incoming flow is laminar, with minimal disturbances, such as air/water flows over wings/turbomachinery, low-speed swimmers, and bluff bodies at low Reynolds numbers. Second, the characteristics of the perturbation can be more easily controlled and maintained for a laminar flow, making it a good configuration to investigate. Finally, and most importantly, triggering instabilities and even turbulence in an otherwise laminar boundary layer significantly enhances the transport of momentum between the near-wall region and the ambient fluid, and serves as an effective means of reducing the extent of separation bubbles.

Separation in turbulent boundary layers (TBLs) is also ubiquitous in external as well as internal flows [11–15]. Examples include the turbulent wake of the canard that serves as the approaching flow for the tail wing; the stream disturbed by the hull of a ship upstream of the rear propeller, and the turbulent duct/pipe flow upstream of a diffuser. However, investigations and control strategies for a turbulent separating flow are much less focused than for a laminar flow and offer additional challenges. First, the laminar-to-turbulent transition mechanism is no longer available to enhance mixing and momentum exchange between the inner and outer regions because the flow is already turbulent. In addition, the diffusive nature of turbulence may lead to a rapid decay of control input and poor receptivity of the perturbation by the boundary layer, making optimal targeted control a challenging goal. For example, a strong control forcing is often required to modify a separating TBL. The momentum coefficient, C_μ, which represents the average momentum input of the control system with respect to the mean momentum of the bulk flow [5], is usually in the order of 10^{-4} to 10^{-2} to reduce the separation region for laminar flows [5,6,8,9]. For turbulent separated flows, pulsed jet actuators with C_μ from 0.25 to 0.4 had to be used [16] to disturb a pressure-induced turbulent separating bubble. Sato *et al.* [17] performed large-eddy simulations (LES) of separation control of flows over a NACA0015 airfoil using dielectric-barrier discharge (DBD) plasma actuators. The C_μ in their study ranged from 5×10^{-5} to 2×10^{-3}. The laminar separation region near the leading edge was significantly reduced by the actuation. However, when the actuator was positioned downstream of the laminar separation region where turbulent separation occurs, no control effect was observed. Sato *et al.* claimed that it was because the fluctuations induced by the actuation immediately vanish due to turbulent dissipation. Cho *et al.* [18] applied a temporal periodic forcing upstream of a turbulent separation bubble (TSB) with $C_\mu = 0.014$. They observed a mild 7% reduction of the separation region at an optimal forcing frequency compared with the uncontrolled flow. Larger separation regions, however, were observed at other forcing frequencies. Another example of the difficulties in further enhancing the turbulent mixing is the effects of surface roughness on turbulent separating flows. As an "inner" disturbance to the flow in the vicinity of the wall, roughness is expected to further enhance mixing and possibly reduce turbulent separating flow. However, early separation was widely reported for separated flow over rough walls in comparison with the smooth-wall cases [19–22]. In spite of the fact that roughness

is known to enhance both the ejection and sweep events for turbulent mixing [23–26], a large mean momentum deficit near the rough wall causes the early separation.

In this paper, we study the control of a turbulent boundary layer using zero-net-mass-flux actuators, with a particular focus on the effects of forcing frequencies as they relate to timescales inherent to the TSB. Existing investigations on the control of separating boundary layers have led to conclusions that do not always agree. There is debate as to whether certain forms of perturbation (frequency, magnitude, waveform, etc.) are optimal for the control of separation. For example, the actuation is often applied at a dimensionless frequency $\text{St} = fL_{\text{sep}}/U_o \sim \mathcal{O}(1)$, where L_{sep} is the length of the uncontrolled mean separation bubble and U_o the freestream velocity. It represents a characteristic period that scales with the time of travel over the streamwise extent of the separation region [27]. Such a frequency scale is also widely denoted as the "vortex-shedding" frequency because it often coincides with the frequency of the most amplified mode of the separated shear layer. Most flow control studies have found that actuation at $\text{St} \sim \mathcal{O}(1)$ reduces the separation region [4]. Mittal and Kotapati [28] reviewed the possibility of a wide optimal range of St from 0.75 to 2.0. Leschziner and Lardeau [29] examined a range of 0.5–1.0 for slot-jet actuators. One problem limiting the application at this Strouhal number is that the natural frequencies of many actuators are usually too high; thus additional low-frequency modulation is needed to achieve $\text{St} \sim \mathcal{O}(1)$.

Researchers have also investigated the response of the separated flow to actuation at higher frequencies [30]. However, there are significant discrepancies in the performance of actuation at large St. Geometry-induced separation, such as in flows around bluff bodies with sharp edges, usually responds more efficiently to a frequency between two to five times the vortex shedding frequency [31]. Some studies on flow separation over an airfoil found that the actuation at $\text{St} = \mathcal{O}(10)$ results in improvement of the aerodynamic performance [32–34]. Meanwhile, many researchers reported the opposite. Among others, Dandois *et al.* [35] performed direct numerical simulation (DNS) and LES of a rounded backward-facing step with zero-net-mass-flux (ZNMF) forcing and noticed that the bubble length was increased by 43 percent at $\text{St} = 4$. Franck and Colonius [36] performed LES of a compressible TBL that separated over the contoured aft part of a wall-mounted hump and reported no reduction in the mean separation bubble length beyond $\text{St} = 5$. The disparities raise the possibility of the confounding nonlinear effects of other parameters besides the actuation frequency—such as geometry dependency, the position of the orifice relative to the nominal separation location in the uncontrolled flow, Reynolds number, etc. Some efforts have therefore been made to limit the dimension of the parameter space. Separating flow over a flat plate, for instance, is one of the configurations that have been used for separating flow studies to avoid the geometry dependency and surface curvature effects [18,22,37,38]. Cho *et al.* [18] performed DNS of a TBL at $\text{Re}_\theta = 300$ over a flat plate. The separation is caused by a freestream suction and blowing velocity profile. Spanwise homogeneous, sinusoidal actuation is applied upstream of the separation point for frequencies up to $\text{St} = 8.75$. They reported that the TSB was fully suppressed for $\text{St} \geqslant 1.56$. Mohammed-Taifour *et al.* [16] conducted several experiments in which a TSB at $\text{Re}_\theta = 5000$ was induced on a flat plate, by applying a contoured roof and suction control on the opposite side of the tunnel. They found that the resulting bubble size was mostly reduced when $\text{St} = 2$–5, while actuation at $\text{St} = 10$ was less effective in limiting the recirculation region.

From this short review, it is clear that the response of separated flows to different actuation frequencies varies significantly due to a vast parameter space related to the flow configuration and actuation type. In the present study, we perform simulations of an adverse-pressure-gradient (APG)-induced separating turbulent boundary layer subjected to streamwise-oriented actuation upstream of the mean separation point. The study focuses on the actuation's ability to promote an instability other than the convective Kelvin-Helmholtz (KH) instability, therefore allowing us to consider alternatives to the usual vortex shedding mechanism. In our recent numerical study on APG-induced separating TBL [39], two types of unsteady modes are observed. One is associated with the KH instability of the separated shear layer, i.e., the vortex shedding mode, which is independent of the length of the separation bubble but scales well with planar mixing-layer laws. The other one is at a frequency that is about 0.4 of the vortex shedding frequency, appearing as the slow formation of a discrete,
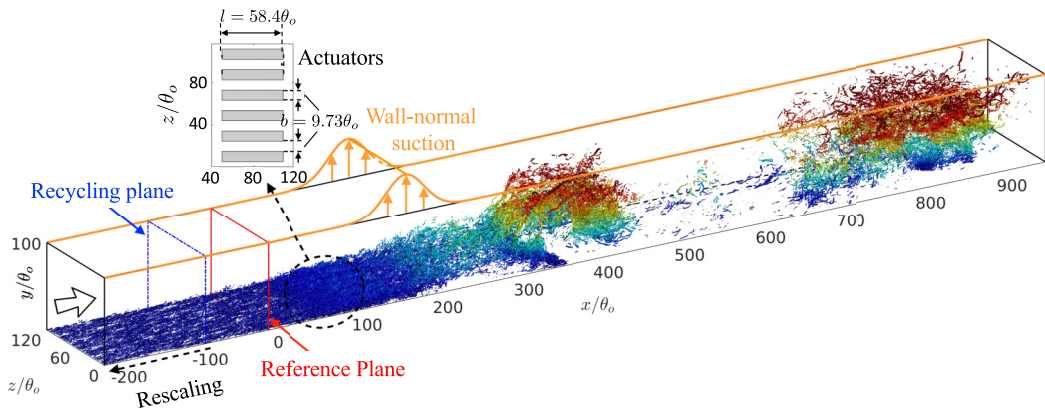
FIG. 1. Schematic of a separating turbulent boundary layer due to freestream adverse pressure gradient. The contours show the instantaneous turbulent structures by isosurfaces of the second invariant of the velocity gradient tensor, colored by the distance from the bottom wall. Also shown are the suction causing the imposed APG in the flow, the actuators as well as the reference and recycling/rescaling planes.

large-scale vorticity packet in the aft portion of the separation bubble. There are also numerous studies on low-frequency motions during flow separation in different types of flows. A common finding of these investigations is that the low-frequency mode carries over 30% of the turbulent kinetic energy [38–42]. Debien *et al.* [43] showed that for separation over a sharp-edge ramp, the best open-loop actuation is at a lower frequency close to that of vortex shedding. They also reported that closed-loop control using a wide range of frequencies has higher optimal actuation frequencies that are close to the KH instability frequency of the shear layer [44]. Being cognizant of the importance of the excitation frequency and the underlying instability, the objective of this study is to shed light on the dynamics of the low-frequency motion during flow separation and the potential to effectively control its extent.

In the following, we first describe the numerical methodology, and then discuss the flow development, as well as the mean-flow features. We then compare the flow response under various actuation frequencies. To complement the simulation results, we also perform a spectral analysis of the harmonic resolvent operator. Finally we draw the main conclusions.

II. PROBLEM FORMULATION

A. Turbulent separating boundary layer

The DNS of the baseline case without control has previously been described in Ref. [39]. While a brief overview of the configuration and simulation methodology is provided here, the reader is referred to Ref. [39] for further details and validation. The simulation employs a rectangular computational domain of length $1170\theta_o$ and height $100\theta_o$ (see Fig. 1), where θ_o is the momentum thickness of the turbulent boundary layer on the bottom wall at a reference plane $203\theta_o$ downstream of the left boundary of the calculation domain. Between $x = 100\theta_o$ and $243\theta_o$ (x, y, and z denote the streamwise, wall-normal, and spanwise directions, respectively), wall-normal suction is applied along the top boundary to impose an APG. Two suction profiles were examined in Ref. [39]. The low-frequency motion was observed when the wall-normal suction velocity profile has one suction peak only. Therefore, this suction-only configuration is employed in the current study. The velocity profile reads

$$V_{\text{top}} = V'_{\text{max}} \exp\left[-\left(\frac{x - x'_c}{\alpha L_y}\right)^2\right], \tag{1}$$
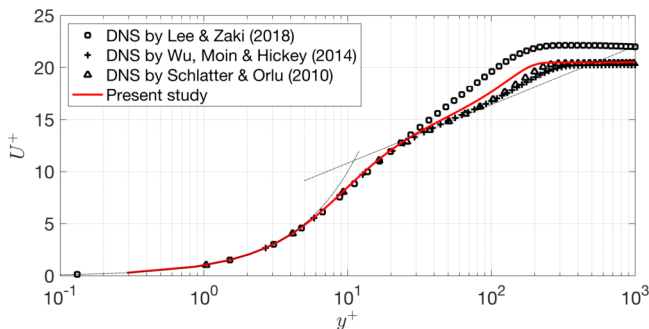
FIG. 2. Comparison of the ZPG TBL generated by the recycling-and-rescaling method by the reference location with other DNS of ZPG TBLs. Square, Lee and Zaki (2018) at $Re_\theta = 500$; cross, DNS by Wu, Moin and Hickey (2014) at $Re_\theta = 670$; triangle, DNS by Schlatter and Örlü (2010) at $Re_\theta = 670$. The current result is at $Re_\theta = 490$.

where $V'_{max}/U_o = 0.9$ (U_o is the freestream streamwise velocity measured at the reference plane), $x'_c/\theta_o = 171.9$, $\alpha = 0.3375$ and $L_y = 100\theta_o$ is the domain height. The pressure gradient created by this suction peaks at the top boundary (refer to Fig. 1) translates into an APG on the wall downstream of the reference plane. At $x = 60\theta_o$ the Clauser pressure gradient parameter [45]

$$\beta = \frac{\delta^*}{\tau_w}\frac{dP_e}{dx} \tag{2}$$

exceeds 0.5 (δ^* is the local displacement thickness; P_e is the pressure measured at the edge of the boundary layer). To obtain a physical zero-pressure-gradient (ZPG) turbulent boundary layer prior to separation, the first $125\theta_o$-long portion of the computational domain ($x \in [-203, -78]\theta_o$) is used for a recycling and rescaling method [46]. The mean velocity and fluctuations at the recycling plane are rescaled to the inlet, using the friction velocity and boundary layer thickness both at the recycling station and at the inlet. Due to the low Reynolds number, the obtained mean velocity profile at the inlet is at $Re_\theta = U_o\theta_o/\nu = 240$ (or $Re_\tau = 110$), which is usually considered as being in the transitional regime. Nevertheless, the recycled-and-rescaled fluctuations act as reasonable disturbances that promote the development of the boundary layer toward a self-similar equilibrium state. By the reference plane ($x = 0$, $203 \theta_o$ downstream of the inlet), the zero-pressure-gradient TBL reaches $Re_\theta = 490$ and $Re_\tau = 200$. The mean velocity at the reference plane shows good agreement with the previous DNS of ZPG TBLs (Fig. 2). The no-slip condition is applied at the bottom boundary and periodic boundary conditions are imposed in the spanwise direction. A convective boundary condition is used at the outflow [47]. Same boundary conditions are used in this investigation for the control cases except at the bottom boundary where the actuations are applied. Details of the actuation will be discussed in the next subsection.

B. Zero-net-mass-flux actuation

Since we focus on modulating the low-frequency motion observed in the uncontrolled flow, it is important to generate structures that such motions can respond to. The dynamics of the low-frequency unsteadiness observed in Ref. [39] are related to the Görtler instability that generates streamwise-elongated structures at the beginning of the separation bubble. Unlike the streaks in the inner layer of a TBL, these structures are usually more than ten times the boundary layer thickness in length and occur in pairs in the homogeneous spanwise direction. Their spanwise wavelength is comparable to the boundary layer thickness. Studies on other forms of separation, such as shock-induced separated flow [48–50], also confirm this mechanism. Therefore, the ability of the actuation to produce perturbations resembling the streamwise-coherent Görtler vortices is

hypothesized to affect the low-frequency motion of the TSB. The topology of the forcing depends strongly on the shape and orientation of the actuator. However, most flow control studies focus on two-dimensional slot actuators with a infinite (or nearly infinite) span to excite the 2D KH instability mechanism. The 2D slot jet is found to form two spanwise homogeneous vortex sheets on the upper and underside of it; the former promotes reattachment, and the latter enhances recirculation. The interaction between the two vortex sheets also generates additional turbulence that enhances mixing [4,51]. Relatively little attention has been paid to other orientations of the actuator orifice. A few investigations reported that round jets are less effective than slot jets, mainly because the widely spaced round jets are too weak to induce large-scale modifications in massive separations [29,52,53]. Slot actuators with their long axis oriented in the streamwise direction are rarely investigated. A few notable studies include the experiments by Smith [54], who observed the formation of streamwise vortices in the boundary layer and higher penetration of the jet into the boundary layer than the spanwise oriented ones. Van Buren *et al.* [55] investigated the formation and evolution of flow structures in a zero-pressure gradient laminar boundary layer. Various orifice pitch and skew angles were tested. Their results confirmed that, compared with other skew angles, the longitudinal (i.e., streamwise) orifice orientation leads to the greatest penetration of the symmetric streamwise vortex pair into the freestream. In addition, a small blockage caused by the jets yielded an increase in the velocity throughout the near-wall region, while a strong crossflow may result in a strong velocity deficit. Similar phenomena are observed in the DNS of streamwise-oriented slots with an attached laminar boundary layer and a separated flow over a hump by Aram and Mittal [56]. They observed that the streamwise-oriented actuator generated a pair of counter-rotating streamwise vortices which constitute the legs of a hairpin vortex. The vortex pair persists for a long streamwise distance from the slot and produces a more substantial downwash ("sweep") of high momentum fluid into the boundary layer.

In this study, streamwise-oriented actuators reviewed above are used to generate streamwise vortices to mimic the streamwise-elongated Görtler vortices that play a critical role in the unsteadiness of the TSBs [39]. The spanwise width and spacing between two adjacent actuators are both set to be $d = 9.67\theta_o \sim \delta_{x=50}$. These are based on the observation in Ref. [39] that the spanwise length scale of the Görtler vortices is comparable to the boundary layer thickness in the TSB without control. The length of the actuators is chosen to match the aspect ratio (i.e., 6:1) in Aram and Mittal [56]. The actuators are placed upstream of the mean separation point between x $= 50\theta_o$ and $108\theta_o$. The zero-net-mass-flux actuation is applied as a sinusoidal wave of the wall-normal velocity described as $V_{ac} = A_{ac} \sin(2\pi f_{ac}t)$, in which subscript $(.)_{ac}$ denotes the parameters of actuation, and A_{ac} and f_{ac} are the magnitude and frequency, and t is time. There is no spanwise actuation and the streamwise velocity component is zero when V_{ac} is positive and has a zero wall-normal gradient when $V_{ac} \leqslant 0$. The same profile has been used in recent studies by the present authors on the effect of actuator modulation schemes on the reduction of a laminar separation bubble to ensure a more realistic velocity distribution near the jet exit [9,57,58]. With this arrangement, the ratio of the ZNMF jet momentum flux to the base flow momentum flux

$$C_\mu = \frac{V_{ac,RMS}^2 N_{ac} d}{U_o^2 L_z} \tag{3}$$

equals to $(A_{ac}/U_o)^2/4$, where $N_{ac} = 6$ is the number of actuation slots in the spanwise direction and L_z the spanwise domain size. The actuation magnitude is chosen to be a small fraction of the freestream velocity because this study focuses particularly on the role of small turbulent structures on flow separation. Large perturbations will likely alter the mean shear directly (e.g., the large velocity deficit reported in Ref. [55]). The choice of small disturbances also allows utilizing the resolvent analysis to explain the dynamics of the TSB. The amplitude is set to be $A_{ac} = 0.05U_o$ and $C_\mu = 6.25 \times 10^{-4}$ in this study. The blowing ratio, defined as [59,60]

$$M = \frac{\text{jet mass flux}}{\text{baseflow mass flux}} = \frac{V_{ac,RMS} N_{ac} d}{U_o L_z}, \tag{4}$$

TABLE I. Simulation parameters.

Cases	$f_{ac}\theta_o/U_o$	$f_{ac}L_{sep}/U_o$	A_{ac}/U_o	x_{sep}	L_{sep}
NA	0	0	0.0	164	450
FL	0.001	0.45	0.05	165	231
FH	0.0025	1.125	0.05	165	274
10FL	0.01	4.5	0.05	163	467

is 0.0176. The actuator array is centered in the spanwise direction to satisfy the spanwise periodic boundary condition. Note that in the undisturbed case, the mean separation occurs at $x = 164\theta_o$ so the centroid (beginning) of the actuator is about 8.7 (11.7) times the local boundary layer thickness upstream of the mean separation point. The Clauser pressure-gradient parameter ranges from 0.4 to 4.1 across the region of the actuator.

Three actuation frequencies are investigated, including the natural frequencies of two characteristic unsteady motions that were observed in Ref. [39]: the low-frequency motion $f_l = 0.001U_o/\theta_o$ and the natural frequency of the shear layer instability (vortex shedding) $f_h = 0.0025U_o/\theta_o$, and an arbitrary high frequency at $10f_l = 0.01U_o/\theta_o$ (or, $4f_h$) [39]. The highest frequency is chosen based on a harmonic resolvent analysis which shows that the mean separation bubble and the low-frequency motion do not respond to the forcing at such actuation frequency. The harmonic resolvent analysis will be described and discussed in more detail in Sec. III E. The corresponding Strouhal numbers based on the uncontrolled TSB length are St = 0.45, 1.125, and 4.5. The nonactuation case is denoted as NA and the three cases with actuation are named FL, FH, and 10FL, respectively (see Table I). Note that, as has been explained in Ref. [39], the vortex shedding frequency gives St = 0.45 in this flow, which is different from other research in which vortex shedding occurs near St = 1 [28,29,37,61,62]. In this flow, the motion close to St $\sim \mathcal{O}(1)$ is the low-frequency generation of discrete large-scale vorticity packet. The mechanisms have been justified with reference to the scaling law of the plane mixing layer and the most amplified Görtler instability [39].

C. Numerical method

The nondimensional, incompressible Navier-Stokes equations for a Newtonian fluid are solved by direct numerical simulation:

$$\frac{\partial u_i}{\partial x_i} = 0, \tag{5}$$

$$\frac{\partial u_i}{\partial t} + \frac{\partial}{\partial x_j}(u_j u_i) = -\frac{\partial p^*}{\partial x_i} + \frac{1}{\text{Re}}\nabla^2 u_i. \tag{6}$$

The equations are normalized by the momentum thickness (θ_o) and freestream streamwise velocity (U_o) at a reference plane that is $203\theta_o$ downstream of the inflow. $p^* = p/(\rho U_o^2)$ is the normalized pressure. The indices 1, 2, and 3 denote the streamwise, wall-normal and spanwise directions, respectively. The corresponding velocity components are u, v, and w.

The same calculation domain and grid as the ones used in our previous study of the undisturbed case are employed, i.e., $1170\theta_o \times 100\theta_o \times 117\theta_o$ and $3072 \times 408 \times 384$ in the streamwise, wall-normal and spanwise directions respectively. The grid resolutions in wall units are $\Delta x^+ = 9.0$, $\Delta y^+(1) = 0.58$ (at the first grid point away from the wall) and $\Delta z^+ = 7.2$ at the reference location and much smaller in the region of the separation bubble, which is sufficient for resolving the near-wall turbulence. This resolution ensures that each actuator is resolved by 153×25 grid points in the $(x - z)$ plane. Away from the wall, the maximum grid spacing (i.e., $\sqrt{\Delta x^2 + \Delta y^2 + \Delta z^2}$) is less than twice the local Kolmogorov scale in all the cases.
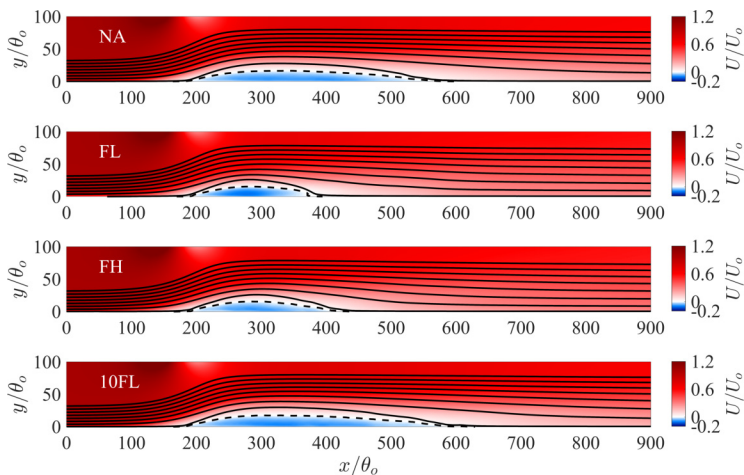
FIG. 3. Contours of the mean streamwise velocity. Solid lines are selected streamlines that pass through $x = 100\theta_o$, $y = [0.2, 5, 10, 15, 20, 25, 30, 35]\theta_o$. Dashed lines show the contour of $U = 0$. From top to bottom: case NA, FL, FH, and 10FL.

To solve the equations, second-order central differencing was used for spatial discretization and second-order Adams-Bashforth semi-implicit time advancement was employed [39,58,63]. The numerical solver was parallelized using the message passing interface (MPI) method [64,65]. The simulations are advanced using a constant time step $\Delta t = 0.03115\theta_o/U_o$ and statistics are collected every 400 time steps over $9000\theta_o/U_o$ after each case reaches its statistically steady state. The maximum CFL number is below 0.4 in all the cases. In the following section, quantities averaged both in time and in the spanwise direction are denoted by capital letters. Other averaging methods are represented by the $\langle.\rangle$ operator.

III. RESULTS

A. Mean flow

The mean-flow distribution is shown in Fig. 3 as contour maps of the averaged streamwise velocity, for the four cases considered. As is evident, the changes in the mean-flow field are significant at certain actuation frequencies. The mean separation bubble is much shorter in the FL and FH cases. Compared with the $450\theta_o$-long mean bubble in the undisturbed case, the location of the mean separation point and the height of the TSB (defined here as the maximum distance between the separating streamline and the wall) barely change between the cases. No significant delayed or early separation is caused by the actuation in this study. The length of the separation bubble at the wall is substantially reduced by the actuation at f_l and f_h, and becomes slightly longer for 10FL (see also Table I). If the effectiveness of flow control is measured by the length of the separation bubble, then our results show that both actuation at the vortex shedding frequency f_h and the one that is 2.5 times lower ($f_l = 0.4f_h$) is effective at significantly reducing the size of the mean TSB. Also, note that the mean TSB of the 10FL case (St = 4.5) is quite similar to the uncontrolled one in the NA case. This result differs from recent observations in Ref. [18] and [16] with similar flow configurations. The discrepancy may be due to the differences in the actuators employed in these studies and the absence of the blowing peak in the freestream in the current study. Such blowing is known to stabilize and constrain the separation bubble dynamics considerably [39]. Two-dimensional infinite slots were used in Ref. [18], in which the TSB was completely avoided for St $\geqslant$ 1.56. Spanwise-oriented slots with an aspect ratio of 6 were used in Refs. [16]. They were also inclined $45°$ to the mean-flow direction. It was found that the optimal frequency range was
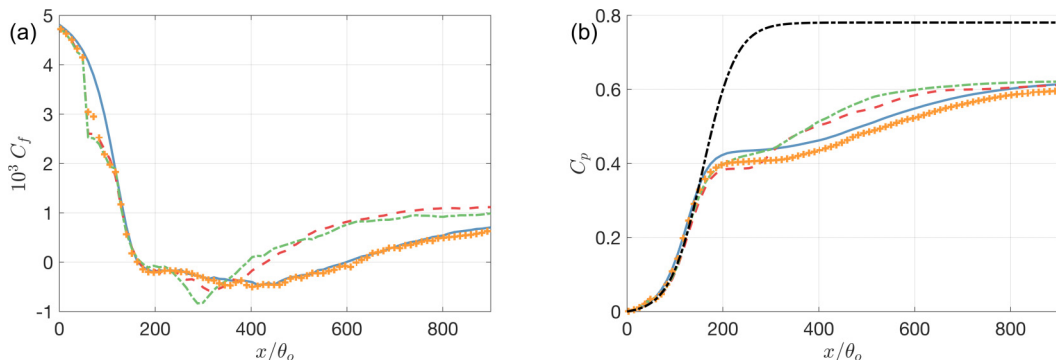
FIG. 4. Mean skin friction coefficient C_f (a) and pressure coefficient C_p (b). —— Case NA, - - - Case FL, —·— Case FH, + Case 10FL. The thick dot-dashed line with a plateau of C_p at $x > 300\theta_0$ in panel (b) is the inviscid pressure profile shown as a reference.

2–$5 f_h$. Besides, the jet velocity in these two studies was 0.50 to $1.05 U_o$, significantly higher than the $0.05 U_o$ used in the present cases.

The mean skin friction coefficient also shows the reduction in the separation bubble length for the FL and FH cases (Fig. 4). Because the mean flow reattaches earlier in these two cases, the region that has a small negative C_f in the uncontrolled case now has a positive skin friction drag, and as a result, the total friction drag over the entire plate ($\int_0^\infty \tau_w dx$) increases. The reversed flow in the vicinity of the wall is slightly stronger in case FH than in case FL. In the next section, these trends will be discussed in light of the turbulent flow structures that appear in these flows. Note that C_f is lower in the actuation region ($x \in [50, 108]\theta_o$) for the three controlled cases because the boundary condition for the streamwise velocity inside the actuator is zero wall-normal gradient for half of the forcing cycle (i.e., when $V_{ac} \leqslant 0$). Quantitatively, the overall skin friction drag per unit span summed up over $x/\theta_o = [0, 900]$ is 0.248 $U_o^2\theta_o$ for case NA (reference value), 0.362 $U_o^2\theta_o$ for FL (+46%), 0.346 $U_o^2\theta_o$ for FH (+40%), and 0.200 $U_o^2\theta_o$ for 10FL (−19%). Note that the partially slip boundary condition at the actuators causes a 0.033 $U_o^2\theta_o$ drag reduction (−13%) in all the control cases. However, form drag dominates the total drag for massive flow separation, like that studied here. As will be discussed momentarily, the FH and FL cases exhibit much better pressure recovery, which would decrease the form drag.

The pressure coefficient (C_p) profiles at the wall in Fig. 4 are compared with the inviscid one obtained by a 2D potential flow calculation. The difference between the actual C_p and the inviscid one is the loss of pressure due to flow separation and skin friction. The profiles show that pressure loss is less in the FL and FH cases downstream of $x = 300\theta_o$ compared with the uncontrolled case due to the early reattachment. Inside the separation bubble, a small amount of pressure is lost by the actuation but in general the pressure recovery is improved at these two excitation frequencies. The 10FL forcing not only slightly increases the length of the mean separation bubble, but also causes more pressure loss at every streamwise location. In internal flow applications such as diffusers, increased pressure recovery is a desirable outcome. Interpretation for external flows such as airfoils is somewhat more complicated: both the increased skin friction and elevated pressure in the FL and FH cases are generally undesirable on the suction side of the airfoil; one type of flow control objectives for airfoils is to have a local modification of the apparent aerodynamic shape of the flow surface—reduce the length and thickness of the nominal airfoil consisting of the actual airfoil and the dead-water separation region—and, as a result, to recover the leading-edge suction peak and/or to fully or partially suppress the flow separation [66]. In the current configuration, all the cases have the same pressure profile near the separation point due to the imposed freestream APG, thus such inviscid effects are not present. Elucidation of how a shorter TSB with a comparable
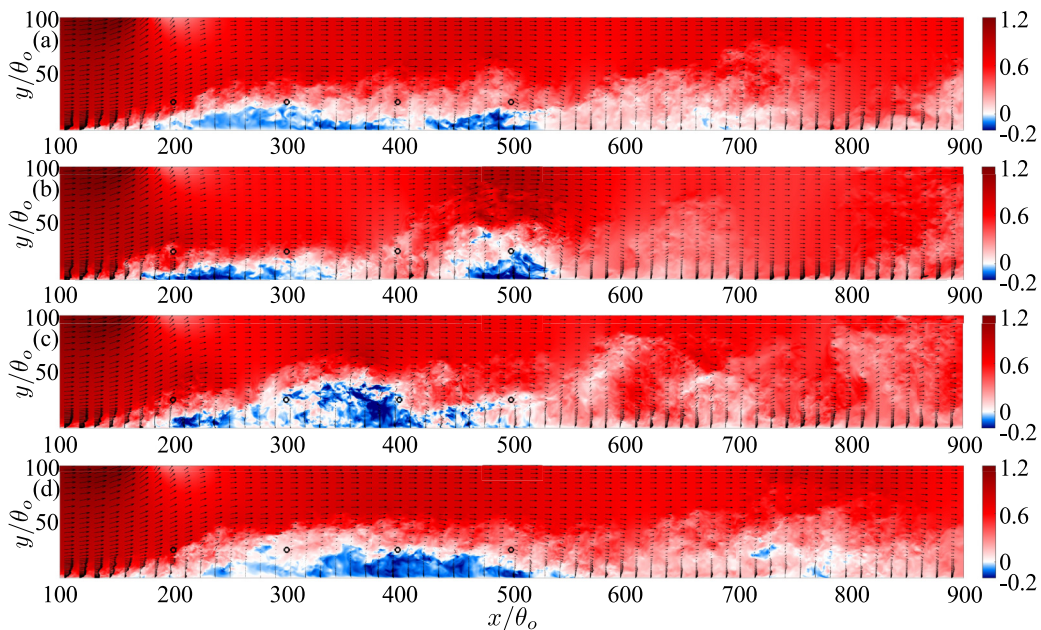
FIG. 5. Instantaneous separating flow shown by the contours of instantaneous streamwise velocity in the middle spanwise section. (a) NA; (b) FL; (c) FH; (d) 10FL. For each case with the actuation, the selected time frame is when $V_{ac} = 0$ and $dV_{ac}/dt < 0$. Also shown are instantaneous velocity vectors on the plane. Circle markers show the locations where the joint-PDFs of velocity fluctuations are examined in Fig. 12.

thickness (thus displacement of the mean flow) can affect the freestream pressure gradient is beyond the scope of the current study.

B. Turbulent structures

Figure 5 shows the contours of instantaneous streamwise velocity in the (x-y) plane in the middle of the spanwise direction. The time instant for each case is chosen to be at half of its corresponding forcing cycle. Similar behavior can be observed regardless of the choice of the examining time frame.

It can be seen that very-large-scale (VLS, radius greater than $50\theta_o$ in this study), clockwise-rotating vortices are formed in the FL and FH cases (e.g., case FL near $x/\theta_0 = 500$ and case FH near $x/\theta_0 = 350$ at the time instant considered). Similar phenomena were also reported in previous studies on flow separation (Refs. [18,32,34,57,67] among others). When the actuation frequency is at $10f_l$, the flow field is very similar to the one in the undisturbed case. Large-scale vorticity packets are also observed in the NA and 10FL (e.g., case NA near $x/\theta_0 = 600$ and case 10FL near $x/\theta_0 = 750$ at the time instant shown). They, however, show much weaker rotation and are less coherent than the ones observed in the FH and FL cases. This indicates that not only the mean but also the stochastic fluctuations of TSB respond differently to various actuation frequencies.

The topology of the turbulent structures are visualized by isosurfaces of the second invariant of the velocity gradient tensor, $Q = -\frac{1}{2}\frac{\partial u_j}{\partial x_i}\frac{\partial u_i}{\partial x_j}$, in Fig. 6. Only the FL and FH cases are shown. The structures of the NA case are depicted in Ref. [39], and for the 10FL case, no apparent difference other than near the actuation region can be identified, hence it is not shown here. Due to the low momentum coefficient and the diffusion of the turbulence, coherent streamwise vortices generated by the actuators are difficult to identify using the Q criterion. However, their footprint can be observed as spanwise-staggered small eddies near the beginning of the separation region.
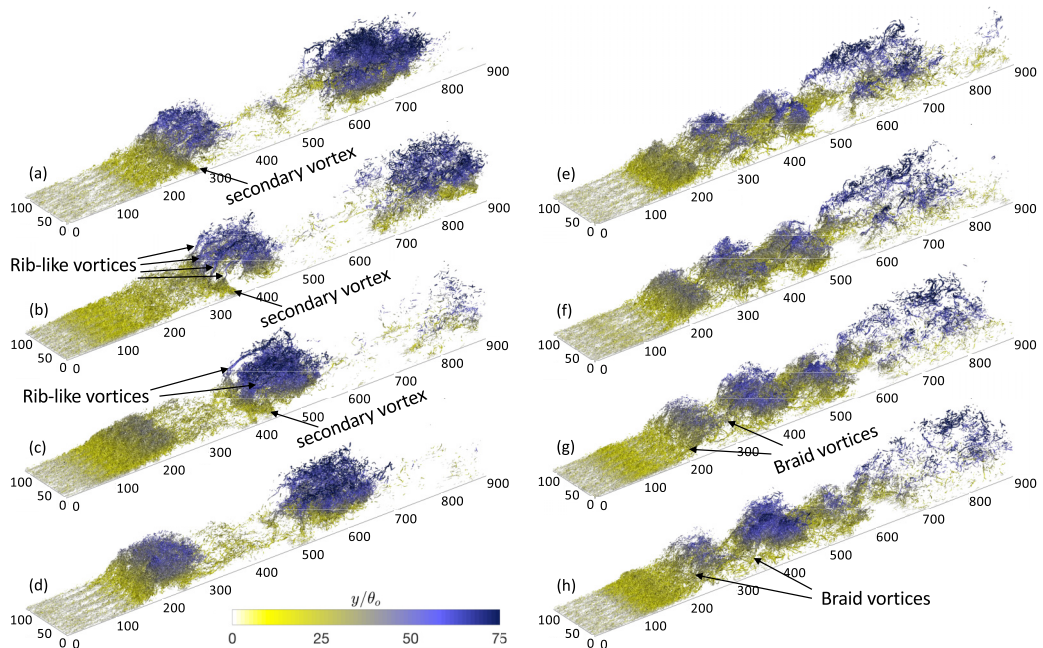
FIG. 6. Instantaneous turbulent structures visualized by isosurfaces of the secondary invariant of the velocity gradient tensor (see text). The isosurface shown is for the threshold $Q = 0.0165U_o^2/\theta_o^2$ and is colored by the distance from the wall. (a–d) FL; (e–h) FH. Top to bottom correspond to time instants $0°$ (a, e), $90°$ (b, f), $180°$ (c, g), and $270°$ (d, h) of the corresponding forcing period in each case.

Instantaneous cross-section flow field visualization confirms the existence of large-scale stochastic streamwise vorticity (not shown). The impact of the streamwise vortices is more prominent when the flow separates because they promote three-dimensionalization. Two distinct features of VLS vortices can be observed: first, in the FL case, a secondary vortex is induced near the bottom wall by the VLS vortex during its formation due to local vortex-induced flow separation. At the beginning of each forcing cycle [Fig. 6(a)], the secondary vortex can be identified as a quasi-2D roller vortex near the wall (at $x = 280\theta_o$ at the time instant shown) rotating in the opposite direction of the VLS vortex. It travels downstream together with the growing VLS vortex even after the latter has shed off from the separated shear layer [Figs. 6(b) and 6(c)]. It decays rapidly and can no longer be identified at a time corresponding to 75% of the forcing period [Fig. 6(d)], a relatively short lifespan compared with the VLS vortex. Second, very-long counter-rotating riblike vortices are formed and rolled around the VLS vortex, especially before the secondary vortex vanishes. They have a length of over $100\theta_o$ in the streamwise direction and cover nearly the entire outer side of the VLS vortex. Ref. [32] also reported a thin concentration of counterclockwise spanwise vorticity near the surface and proposed that it may accelerate the loss of phase coherence.

The structures and dynamics observed here thus correspond to a secondary vortex and the formation of a vortex pair by the VLS vortex and the secondary vortex. It is very similar to the vortex pair observed in impinging jets, where a vortex ring that strikes the surface causes local flow separation and the formation of a secondary, counter-rotating vortex [21,68–70]. Wu and Piomelli [70] studied the interaction between impinging vortex rings and a radial wall jet. The vortex ring (named "primary vortex") and the secondary vortex it induced form a vortex pair that travels downstream together. The turbulent diffusion caused by the interaction between the primary and secondary vortices is the key sink term in the spanwise vorticity budgets. Another factor that facilitates the decay of the primary vortex was identified in Ref. [70] as a secondary instability
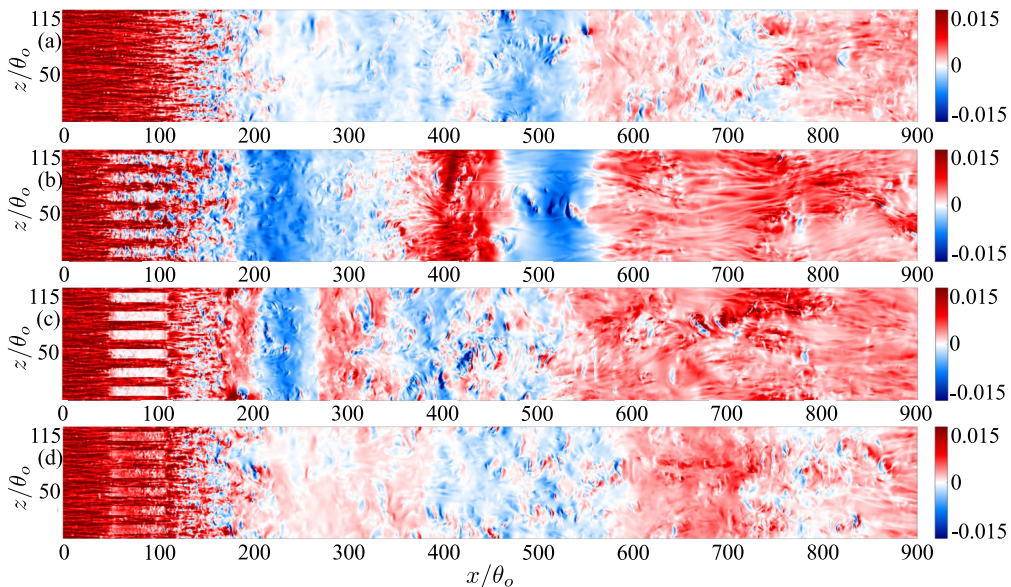
FIG. 7. Contours of instantaneous streamwise velocity on the (*x*-*z*) plane corresponding to the first DNS grid point away from the wall. (a) NA; (b) FL; (c) FH; (d) 10FL. The time frame shown for each case is the same as the one shown in Fig. 5.

appearing as riblike vortices rolled around the vortex pair. Similar phenomena were also reported in Otsuka *et al.*'s [71] investigation of sediment suspension by organized vortices produced under breaking waves in the surf zone. Both the formation of the secondary vortex by local vortex-induced separation and the riblike vortices are in good qualitative agreement with the phenomena observed in the FL case. It indicates that vortex-dominant local separation is the common mechanism shared by these flow configurations. The secondary vortex and riblike vortices are not seen in the FH case [Figs. 6(e) and 6(h)]; however, the structures between consecutive VLS vortices at this excitation frequency are very similar to the streamwise braid vortices observed in jets or vortex streets in the shear layer between two successive vortices [72,73].

Comparing the FL and FH cases, the streamwise distance between consecutive vortices increases when the actuation frequency decreases. For example, at the last time instant showed [Figs. 6(d) and 6(h)], one VLS vortex is centered at $x = 425\theta_o$ in the FH case, while a new one is near $x = 280\theta_o$. The streamwise distance between the two is $145\theta_o$. For FL, for comparison, the old VLS vortex is at $x = 550\theta_o$ while a new one appears at $x = 240\theta_o$. The streamwise distance between the two is $310\theta_o$. Recall that the ratio of the two frequencies is $f_h/f_l=2.5$. If the VLS vortices in the two cases are convected by the same ambient velocity, then the ratio between these two distances should be equal to the ratio of the forcing period ($T_h/T_l = f_l/f_h = 1/2.5 = 0.4$). Indeed, the value shown here is 0.47. It indicates that the convective velocities of the VLS in the two cases are roughly equal because the actuation is ZNMF.

Contours of the streamwise velocity at the first grid point away from the wall are shown in Fig. 7 at the same time frames as in Fig. 5. The footprints of the VLS vortices can be seen near the wall as the light-color, spanwise-coherent zones in the figure. Despite the fact that the actuation has variations in the spanwise direction, the large-scale features of the VLS vortices in the FL and FH cases are quite two-dimensional, with little variance in the spanwise direction after they are just formed. A possible reason for this spanwise coherence is that the six actuators act temporally in phase. Some wiggles over these mainly 2D regions appear more rapidly in the FH case than in the FL case. The forward-flow region between consecutive VLS vortices shows a large magnitude of *u*
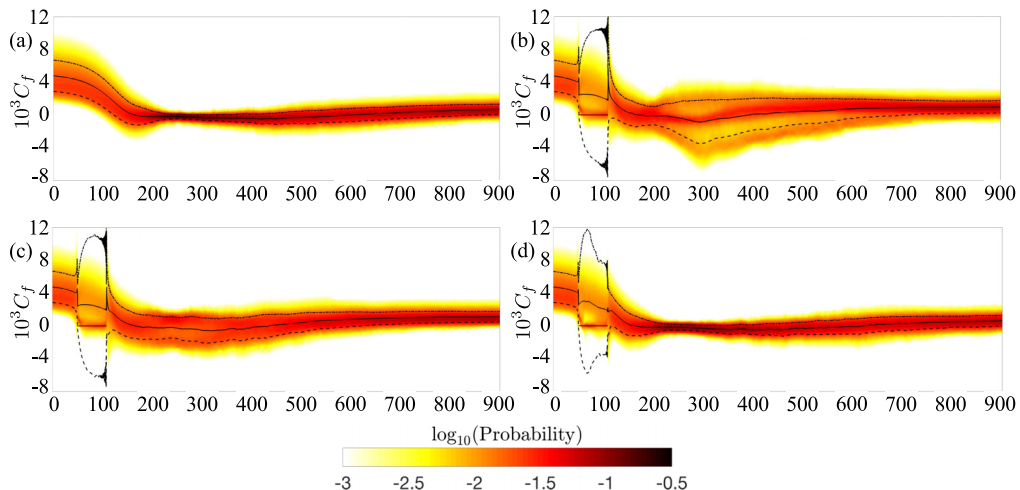
FIG. 8. Probability density function of the instantaneous, local friction coefficient as function of downstream distance. The mean C_f of each case and range of its root-mean-square value are also plotted for reference as solid and dashed lines. (a) NA; (b) FL; (c) FH; (d) 10FL. The actuation region is $x \in [50, \ 108]\theta_o$.

in the FL cases [$x = 400\theta_o$ in Fig. 7(b)], representing the formation of the secondary vortex. The signature of the riblike vortices is also noticeable. Further downstream of the previous VLS vortex, the spanwise coherence of the flow vanishes, and long streamwise streaks appear near the wall (e.g., $x = 600$–$800\theta_o$ in the FL case and $x = 540$–$750\theta_o$ in the FH case at the showing time instants). This is where the flow tends to recover toward the canonical turbulent boundary layer (see also the vector fields shown in Fig. 5).

Note that information about the strong temporal variability of near-wall flow caused by the VLS vortices is not contained in the mean quantities. In the mean C_f profile (Fig. 4), the reversed flow in the vicinity of the wall is slightly stronger in FH than in FL, even though the instantaneous fields indicate stronger VLS vortices in the latter (thus a higher reversed flow due to the rotation). Based on the discussion above, it is likely that the strong negative local C_f is averaged out by the positive C_f from the secondary vortex in the FL case. To characterize the temporal variability more quantitatively, we examine the probability of instantaneous, local $C_f = \tau_w/(1/2\rho U_o^2)$ where τ_w is the instantaneous wall shear stress on the wall (Fig. 8). The instantaneous C_f has a much broader probability distribution in the FL and FH cases in the region $x \in [200, 400]\theta_o$ compared with a narrow peak in the NA and 10FL cases, leading to a larger fluctuation in the local C_f. In particular, the FL case shows three local peaks in the map around $x = 300\theta_o$ while the FH case has two. The low-C_f peak reaches $C_f = -4 \times 10^{-3}$ in the FL case and -2×10^{-3} in FH, consistent with the earlier observation that the VLS vortex has stronger clockwise rotation in the FL case than in FH (refer to Fig. 7). The positive, high C_f peak in the FL case also shows a larger magnitude than the one in the FH case. The two opposite peaks cancel more in the FL case than in the FH case, leading to the false impression that the latter contains a stronger local separation. The profile of the probability at $x = 300\theta_o$ is plotted in Fig. 9(a). In engineering applications, the unsteady, extreme skin friction load may cause sudden aerodynamic overheating, noise, vibration, and off-design operation, which should be a critical factor that needs attention during design. Therefore, in spite of the fact that the actuation used in this study is able to significantly reduce the mean separation size, it should be kept in mind that it might enhance the unsteadiness of flow separation.
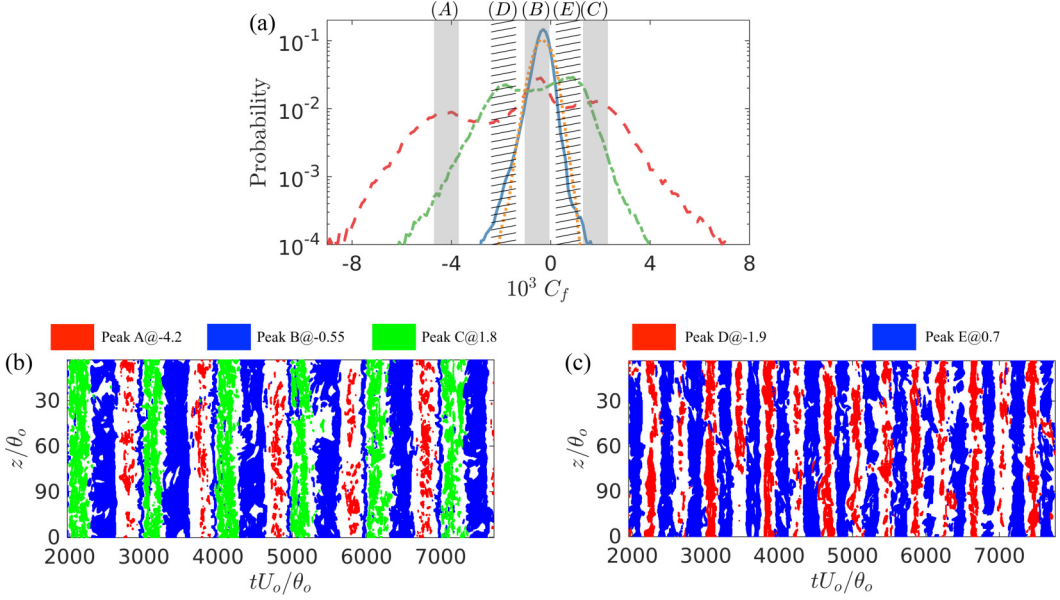
FIG. 9. (a) Probability density function of the instantaneous, local friction coefficient at $x = 300\theta_o$. ——, case NA; – – –, case FL; –·–·–, case FH – – –, case 10FL. (b, c) visualizations of the instantaneous distribution of C_f when values near the peaks of the PDFs shown in panel (a). (b) Case FL, peak A, red; peak B, blue; peak C, green. (c) Case FH, peak D, red; peak E, blue. $C_{f,\text{peak}\pm0.5}$ is used as condition near each peak, i.e., filled (FL) and hatched (FH) patches in panel (a).

C. Unsteadiness

Using the PDF of instantaneous C_f, we investigate the flow field that corresponds to each peak in the map to characterize the unsteadiness quantitatively, especially for the FL and FH cases where multiple peaks appear at the same x location. We use conditional averaging based on the condition that the instantaneous, local C_f falls within a range of $\pm5 \times 10^{-4}$ around the peaks. We show such events in the temporal-spanwise map at $x = 300\theta_o$ (Fig. 9). For the FL case, the three peaks are at $C_f = [-4.2, -0.55, 1.8] \times 10^{-3}$ (denoted here as Peak A, B, and C). The (t-z) map consists of spanwise blocks in each forcing cycle corresponding to the passage of the vortex pair at this streamwise location. The block of peak C represents the forward near-wall flow by the counterclockwise-rotating secondary vortex; peak A is the front of the VLS vortex that is striking the surface; peak B appears as two regions on the map, a long-lasting one (named B_l) represents the rear end of the VLS vortex (or the interval between successive VLS vortices), and a short-lasting one (named B_s) between peak A and C. Therefore, a sequence of Peak $A \rightarrow B_s \rightarrow C \rightarrow B_l$ represents the actual vortex shedding cycle. This map confirms that both the VLS vortex and the secondary vortex are coherent in the spanwise direction, especially the latter one. In contrast, the FH case only has two peaks close to zero ($C_f = [-1.9, 0.7] \times 10^{-3}$, denoted as peaks D and E respectively). The VLS vortex produces a narrower reversed flow near the wall than in the FL case. Secondary vortices may not form at all in case FH because no qualitative difference can be identified between the nearly zero C_f regions before and after the block of peak D.

Due to the large-scale unsteadiness during flow separation, the size of the separation bubble varies significantly in time. Figure 10 plots the history of the total reversed flow area in the (x-y) plane, i.e., $A_{r,xy} = \int_{\Omega_r} dx dy$, where Ω_r denotes the region where $\langle u \rangle_z < 0$. The transient period from the initial undisturbed TSB to the statistical steady state is also shown on the negative portion of the t axis. We observed in our previous study that there is a large-amplitude, low-frequency variation of $A_{r,xy}$ in the NA case (solid line) [39]. With the actuation on, the FL and FH cases show
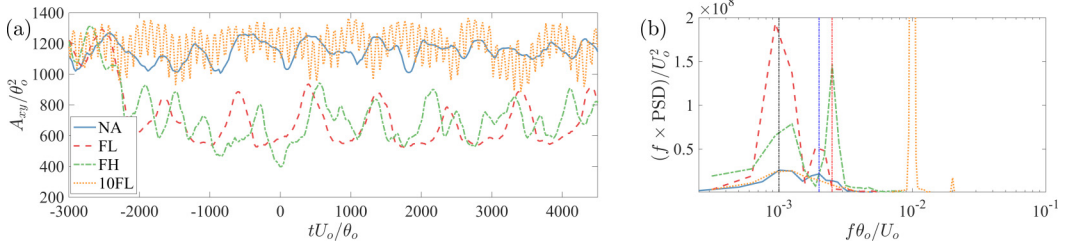
FIG. 10. Time history of the total area of the recirculation region in the $(x$-$y)$ plane between $x = 0$ and $x = 500\theta_o$ (a) and its premultiplied energy spectrum (b). The instant shown as $t = 0$ in panel (a) is approximately when a statistically steady state is reached after the transition from the initial undisturbed field. Thin vertical lines indicate the three natural frequencies of the undisturbed TSB [39].

a significant reduction in $A_{r,xy}$ and 10FL actuation does not change the mean $A_{r,xy}$ much. The root-mean-square of $A_{r,xy}$ is nearly doubled by the actuation regardless of the actuation frequency. The footprint of the periodic actuation is clearly seen from the variation of $A_{r,xy}$ for the three controlled cases. Moreover, the large-amplitude, low-frequency modulation still exists regardless of the forcing frequency, as further confirmed by the premultiplied energy spectrum of $A_{r,xy}$ shown in Fig. 10(b). The low-frequency peak persists in all cases.

D. Turbulent statistics

Contours of the turbulent kinetic energy (TKE) (averaged both in time and in the spanwise direction) are plotted in Fig. 11. The TKE is increased by a factor of 2 to 3 in the FL and FH cases especially downstream of $x = 200\theta$ where the VLS vortex is formed. For the FL case, the highest
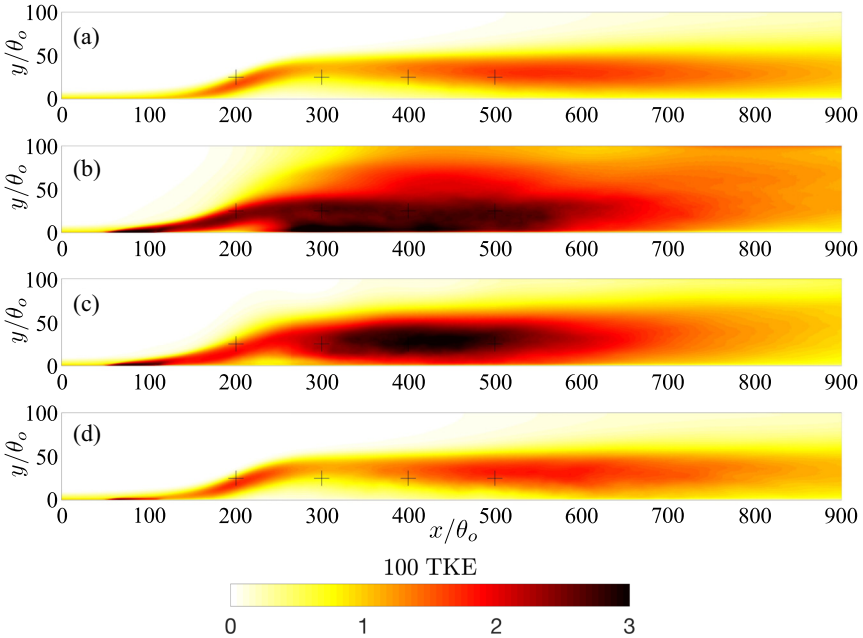

FIG. 11. Contours of the turbulent kinetic energy. The locations where the joint probability density function of u' and v' are examined are marked by $+$. (a) NA; (b) FL; (c) FH; (d) 10FL.
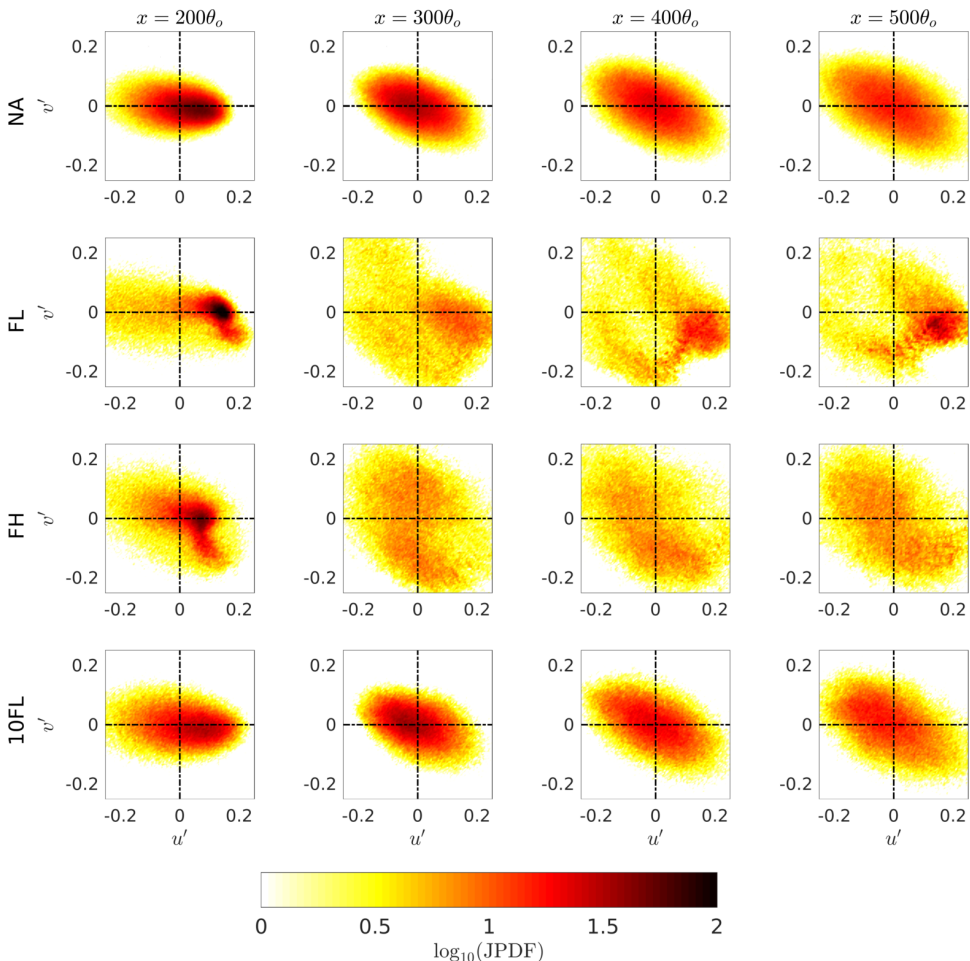
FIG. 12. Contours of JPDF of streamwise and wall-normal velocity fluctuations for the four cases (one in each row). The JPDFs are examined at $y/\theta_o = 25$ and four streamwise locations (one in each column). The bin size is $0.005 U_o$. The JPDF is calculated using 500 snapshots and all the DNS grid points in the spanwise direction, at each x location.

TKE occurs near the wall between $x = 250\theta_o$ and $500\theta_o$. It is the region where the secondary vortex is formed before decaying. This region is not observed in the other three cases. Case 10FL has a very similar TKE distribution and magnitude as the NA case. No change can be identified even before the TBL separates ($x = 150\theta_o$) or at the beginning of the separated shear layer ($x = 200\theta_o$). The high-frequency actuation appears to leave the incoming TBL turbulence mostly unaffected.

The ability to delay flow separation (or promote the reattachment) is closely related to the process of bringing high-momentum fluid from the freestream to the near-wall region to compensate the momentum deficit caused by the APG. For canonical TBLs, such momentum transfer is caused by the sweep events that are associated with positive streamwise fluctuations being moved toward the wall by the hairpin vortices in the inner layer. It has been widely reported in the literature that the outer layer of the TBL responds to the APG even before flow separation. A secondary peak appears in the Reynolds stress profile, causing a significant production of TKE in the outer region [23]. Meanwhile, the anisotropy of the near-wall turbulence is reduced as the sweep events become dominant [74].
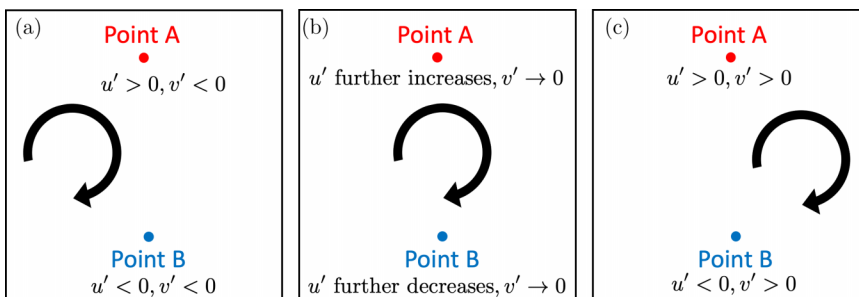
FIG. 13. Schematics of the vortex-induced velocity fluctuation. Point A (B), a location that is above (underneath) the trajectory of the primary vortex. From (a) to (c), time instants that the vortex is approaching and passing Points A and B.

The discussion in the previous sections shows that the actuation employed in the current configuration does not affect the mean separation point, but decreases the size of the TSB at certain frequencies. It means that the additional vertical momentum transfer by the added streamwise vortices is still insufficient to act against the APG in this flow to delay the flow separation. What the actuation alters here is the instability and vortex topology in the separated shear layer, thus modifying the reattachment point downstream. That is, the structures generated after flow separation appear critical in determining the length of the separation bubble. Therefore, we now focus the attention to the outer layer structures, i.e., the clockwise rotating vortices generated by the separated shear layer, over the separation region.

The joint probability-density-function (JPDF) of the fluctuating streamwise and wall-normal velocity components are examined at several x locations (see Fig. 12, refer to Figs. 5 and 11). The wall-normal distance between the monitoring locations and the wall is chosen to be $25\theta_o$. The choice is made because (1) it is in the middle of the separated shear layer at $x = 200\theta_o$ (refer to Fig. 11); (2) the high-TKE region further downstream, which corresponds to the trajectory of the VLS vortices, is also about $25\theta_o$ away from the wall; (3) this height is above the region related to the secondary vortex in the FL cases, thus focusing our attention on the VLS vortex. At $x = 200\theta_o$, the JPDFs in all the cases have an elongated shape with a long axis along the u' axis. All four cases at $x = 200\theta_o$ also show a dominant peak at positive u' and $v' \sim 0$. Streamwise-elongated structures are formed either by the Götler instability or by the actuation in this region and lead to a dominant u' component. In the FL and FH cases, the dominance of this peak is more prominent and it locates at higher u', indicating that the vortices are more energized. A secondary peak near the lower-right corner of the peak (i.e., at slightly higher u' and negative v' than the peak) appears in the FL and FH cases, which is likely associated with secondary structures caused by the actuation that brings additional high-momentum from the freestream to the separated shear layer.

Further downstream at $x = 300\text{--}500\theta_o$, the JPDFs of the NA and 10FL cases recover to the canonical (Q_2–Q_4)-inclined ellipse. It, however, changes significantly in the FL and FH cases. Instead of a (Q_2–Q_4)-inclined ellipse, the JPDF in the FL case shows a distinct peak at high positive u' and negative v', along with several ridges in each quadrant. These features can be associated with the sequence during the passage of the large-scale vortex shown in Fig. 7. Focusing on a point below the trajectory of the VLS vortices and a new vortex is formed upstream of this position, rotating clockwise (Point B in Fig. 13). Due to the rotation of the vortex, when this vortex approaches the point in question [Fig. 13(a)], the point B first experiences a negative v' and a negative u' induced by the rotation of the vortex (Q3); as the vortex travels downstream [Fig. 13(b)], u' becomes more and more negative and the negative v' decreases (along the ridge in Q3, from the negative y axis to negative x axis), until the center of the vortex passes above the point B. After that, u' remains negative but its magnitude decreases, while v' becomes positive with an increasing magnitude (along the ridge in Q2, from the negative x axis to the positive y axis) [Fig. 13(c)]. However, if

the considered point is located above the VLS path (Point A in Fig. 13), then it will first experience a large negative (and, decreasing) v' and a positive (increasing) u' (along the ridge in Q4 from the negative y axis to the positive x axis), and then a positive (increasing) v' and a positive (decreasing) u' (along the ridge in Q1 from the positive x axis to the positive y axis) after the center of the vortex pass it in the streamwise direction. Note that Points A and B are actually the same examining location for each JPDF; the change of its relative position with respect to the VLS is due to the unsteadiness of the flow and the inhomogeneity of VLS in the spanwise direction.

Taking into account that the vortex is evolving as it travels downstream, the missing positive v' branch in the JPDF of the FL case may be related to the fact that the vortex is decaying as it passes the analysis locations. Also note that the scenario described here only applies in a statistical (conditionally averaged) sense. Instantaneous histories at a particular location do not follow a well-defined trajectory along the ridges on this map because the VLS vortex is highly variable in this turbulent flow. This JPDF map is using the data at all the grid points in the spanwise direction at many time instants thus representing a statistical view of the process. For the FL case, the dominant peak of the JPDF in Q4 near the positive x axis indicates that the analysis location is above the (most likely) pathline of the vortex core and the vortical structure is most coherent (leading to a higher JPDF) when the center of the vortex is approaching but has not yet passed the analysis point.

Compared with the FL case, the FH case does not show a clear pattern in the JPDF map. The shape is slightly different from the canonical (Q_2–Q_4)-inclined ellipse observed in the NA and 10FL cases at $x = 300\theta_o$ while further downstream it rapidly recovers toward the ellipse without a distinct peak. It may be due to the relatively weak VLS vortices formed in this case that lose their coherence more rapidly than the ones in the FL case and become a diffusive shear layer as the one in the NA and 10FL cases.

E. Linear harmonic resolvent analysis

In this section we perform the linear harmonic resolvent analysis, which was developed in Ref. [75] to study the cross-frequency interactions in nonlinear, unsteady flows. We will see that the results from this linear analysis support our observations regarding the receptivity and response of the flow to actuation at different frequencies. The method is briefly introduced here. The readers are referred to Ref. [75] for additional details.

Let $\mathbf{q}(t) = (\mathbf{u}(t), p(t))$, denote the state vector containing the three-dimensional vector velocity $\mathbf{u}$ and the scalar pressure field p. The harmonic resolvent analysis is concerned with the analysis of the dynamics of small perturbations $\mathbf{q}'(t)$ about a base flow $\mathbf{Q}(t) = \mathbf{Q}(t + T)$ that is time-periodic with period T. Upon linearization of the Navier-Stokes equation and of the continuity equation about $\mathbf{Q}(t)$, one obtains a linear periodically time-varying system of the form

$$\underbrace{\begin{bmatrix} \mathbf{I} & 0 \\ 0 & 0 \end{bmatrix}}_{\mathbf{M}} \partial_t \mathbf{q}'(t) = \mathbf{A}(\mathbf{t}; \mathbf{Q}(\mathbf{t}))\mathbf{q}'(\mathbf{t}) + \mathbf{f}'(\mathbf{t}), \tag{7}$$

where $\mathbf{A}(\mathbf{t}; \mathbf{Q}(\mathbf{t}))$ is a T-periodic linear operator whose periodicity is inherited from the base flow $\mathbf{Q}(t)$. The vector $\mathbf{f}'(t)$ contains higher-order terms $O(\|\mathbf{q}'(t)\|^2)$ coming from the linearization of the Navier-Stokes equation about $\mathbf{Q}(t)$. Since $\mathbf{A}(t)$ is periodic, it can be expanded into a Fourier series with fundamental frequency $\omega = 2\pi/T$,

$$\mathbf{A}(t) = \sum_{k\omega\in\Omega_b} \hat{\mathbf{A}}_k e^{ik\omega t}, \quad \Omega_b = \omega\{-r_b, \cdots, 0, \cdots, r_b\}. \tag{8}$$

Here, Ω_b is the set of frequencies associated with $\mathbf{A}(t)$ and r_b is a positive integer. We now seek solutions $\mathbf{q}'(t)$ to Eq. (7) of the form

$$\mathbf{q}'(t) = \sum_{k\omega\in\Omega} \hat{\mathbf{q}}_k e^{ik\omega t}, \quad \Omega = \omega\{-r, \cdots, 0, \cdots, r\}. \tag{9}$$

The set Ω is the set of frequencies associated with the perturbations $\mathbf{q}'(t)$ and $r \geqslant r_b$ is a positive integer that is chosen according to the physics of the problem of interest. Plugging Eqs. (8) and (9) into Eq. (7), and writing $\mathbf{f}'(t)$ in a Fourier series over Ω as in Eq. (9), the equation can be written as

$$\mathbf{T}\hat{\mathbf{q}}' = \hat{\mathbf{f}}', \tag{10}$$

where $\hat{\mathbf{q}}' = \{\hat{\mathbf{q}}'_k\}_{k\omega \in \Omega}$ denotes the collection of all Fourier coefficients of $\mathbf{q}'(t)$ and $\hat{\mathbf{f}}'$ is defined similarly. The operator $\mathbf{T}$, on the other hand, is given by

$$[\mathbf{T}\hat{\mathbf{q}}']_k = ik\omega\mathbf{M} - \sum_{j\omega \in \Omega} \hat{\mathbf{A}}_{k-j}\hat{\mathbf{q}}'_j. \tag{11}$$

Note that Eq. (10) is a system of linearly coupled equations, where the coupling between the flow structure $\hat{\mathbf{q}}'_k$ at frequency $k\omega \in \Omega$ and the flow structure $\hat{\mathbf{q}}'_j$ at frequency $j\omega \in \Omega$ happens via the base flow $\hat{\mathbf{A}}_{k-j}$ at the frequency difference $(k - j)\omega \in \Omega_b$. It is precisely the time-varying nature of the base flow that allows for cross-frequency coupling between different flow structures. If the base flow was steady (e.g., the temporal mean or a steady solution of the Navier-Stokes equation), then the linearized Navier-Stokes Eq. (7) would be a linear time-invariant (LTI) system, and it is well-known that LTI systems do not support cross-frequency coupling. It is also worth observing that LTI systems lead to the well-known mean-based resolvent analysis described in Refs. [76,77].

Finally, resuming from Eq. (10), the harmonic resolvent operator $\mathbf{H}$ is defined as a linear operator that maps inputs $\hat{\mathbf{f}}'$ to outputs $\hat{\mathbf{q}}'$ according to

$$\hat{\mathbf{q}}' = \mathbf{H}\hat{\mathbf{f}}', \quad \text{Range}(\mathbf{H}) \perp \mathbf{v}, \tag{12}$$

where $\mathbf{v}$ is a unit-norm vector pointing in the direction of a phase shift about the base flow $\mathbf{Q}(t)$. In general, $\mathbf{H}$ cannot be defined as the inverse of $\mathbf{T}$, since this may not exist. We refer to Ref. [75] for a more thorough explanation.

The singular value decomposition of the harmonic resolvent operator sheds light onto the input-output mechanisms of the flow. In particular, the first right singular vector of $\mathbf{H}$ provides information on the forcing input $\hat{\mathbf{f}}'$ that excites the most amplified response $\hat{\mathbf{q}}'$. The most amplified response, however, is spanned by the first left singular vector of $\mathbf{H}$. The first singular value can be understood as a gain on the first input-output vector pair. Now, let $\mathbf{H}_{k,j}$ denote the block of the harmonic resolvent that maps inputs $\hat{\mathbf{f}}_j$ at frequency $j\omega$ to outputs $\hat{\mathbf{q}}'_k$ at frequency $k\omega$. It can be shown that the singular value decomposition of $\mathbf{H}_{k,j}$ sheds light on the input-output mechanisms between the two frequencies of interest. The first right and left singular vectors of this block of the harmonic resolvent can be interpreted in a similar fashion as before. The first singular value can be used to quantify how strongly an input at frequency $j\omega$ affects the response at frequency $k\omega$.

This framework is applied to the turbulent separation bubble to quantify the receptivity of the flow to actuation at different frequencies. To obtain the base flow, we first spanwise-average the data generated from the *uncontrolled* direct numerical simulation (case NA). This will yield a spatially two-dimensional, time-dependent vector $\mathbf{Q}(x, y, t) = (U(x, y, t), V(x, y, t), P(x, y, t))$ where U and V denote the streamwise and wall-normal components of velocity and P denotes the pressure. In this analysis, we examined the dynamics of small perturbations about the large, coherent structures that oscillate at the low breathing frequency $\omega = 2\pi f_l$, where $f_l = 0.001$. Therefore, the base flow for the harmonic resolvent analysis is defined by setting $\Omega_b = \omega\{-1, 0, 1\}$ for $\mathbf{Q}$ in Eq. (8). The Fourier modes $\hat{\mathbf{Q}}_k(x, y)$ are shown in Fig. 14. The figure shows that the mean flow (a, b) is much more energetic than the structures that oscillate at the breathing frequency ω (c, d). However, including the unsteady component in the base flow allows us account for the cross-frequency coupling that determines the response of the TSB to actuation at different frequencies. The harmonic resolvent analysis described above is then performed by considering two-dimensional perturbations $\mathbf{q}'(x, y, t) = (u'(x, y, t), v'(x, y, t), p'(x, y, t))$ over the set of frequencies $\Omega = \omega\{-10, \cdots, 0, \cdots, 10\}$ in Eq. (9). The linearized Navier-Stokes equation is discretized using second-order finite differences on a fully staggered spatial grid of size $N_x \times N_y = 1270 \times 205$, and
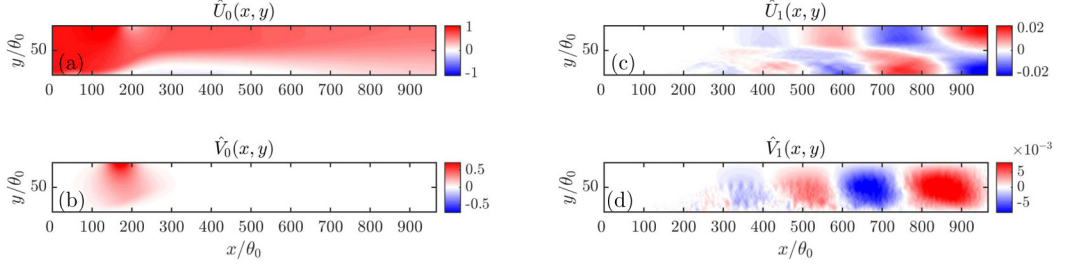
FIG. 14. (a, b) Time-averaged streamwise and wall-normal velocities used as the zero-frequency component of the base flow. (c, d) Streamwise and wall-normal velocities from the Fourier mode $\hat{\mathbf{Q}}_1$ associated with the breathing frequency f_l.

then the matrix $\hat{\mathbf{T}}$ defined in Eq. (11) is assembled. Since there are 21 frequencies in the set Ω and the vector $\mathbf{q}'(x, y, t)$ contains two velocity components alongside the pressure, this matrix will have size $N = 21 \times 3 \times (N_x \times N_y) \approx 1.63 \times 10^7$, but it will be very sparse. Finally, we compute a rank-m singular value decomposition of the harmonic resolvent and of all its blocks. Respectively, we have

$$\mathbf{H} = \sum_{l=1}^{m} \sigma_l \hat{\phi}_l \hat{\psi}_l^*, \quad \mathbf{H}_{k,j} = \sum_{l=1}^{m} \lambda_{(k,j),l} \hat{\phi}_{(k,l)} \hat{\psi}_{(j,l)}^*. \tag{13}$$

This calculation is performed using one of the randomized algorithms described in Ref. [78] by an in-house PETSc-based solver.

Figure 15(a) shows the leading $m = 10$ singular values of the harmonic resolvent $\mathbf{H}$, while Fig. 15(b) shows the leading singular value $\lambda_{(k,j),1}$ of each block $\mathbf{H}_{k,j}$. From Fig. 15(a) we learn that the harmonic resolvent is low rank, since the leading singular value σ_1 is larger than σ_{10} by more than one order of magnitude. The map in Fig. 15(b) shows which frequency pairs $(k\omega, j\omega)$ are more strongly coupled. In particular, since we are interested in how external perturbations influence the mean separation bubble and the low-frequency unsteadiness, we will focus on the 0ω and 1ω rows of the map in Fig. 15(b). It is observed that the zero-frequency component of the flow (i.e., the mean flow) is affected by perturbations at frequencies ω up to 5ω. This is in agreement with what was observed via the direct numerical simulations. By contrast, the zero-frequency
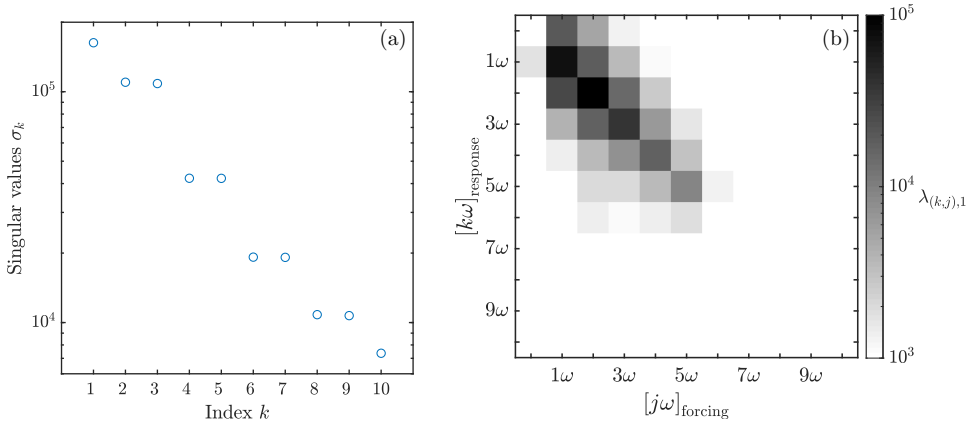

FIG. 15. (a) Leading $m = 10$ singular values of harmonic resolvent operator $\mathbf{H}$. (b) Leading singular value $\lambda_{(k,j),1}$ computed for the blocks $\mathbf{H}_{k,j}$ of the harmonic resolvent operator.
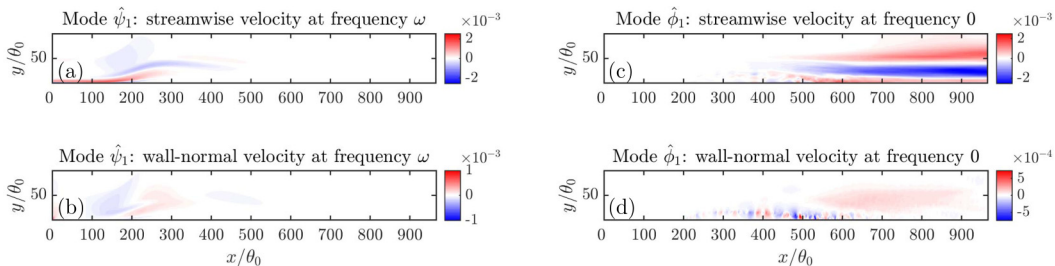
FIG. 16. (a) The optimal streamwise velocity as the control input at frequency ω, extracted from the first right singular vector $\hat{\psi}_1$ of $\mathbf{H}$. (b) the most significant response of the streamwise velocity at frequency 0 (i.e., the mean flow), extracted from the first left singular vector $\hat{\phi}_1$ of $\mathbf{H}$.

component is unaffected by external perturbations at higher frequencies, say 10ω. This is also in good agreement with the findings of the simulation. Similarly, the low-frequency unsteadiness (row 1ω) is affected by perturbations at frequencies up to 5ω. Once again, this is consistent with our numerical studies, where we found that forcing at frequency 2.5ω generated high-energy flow structures at the (fundamental) low frequency 1ω.

Figures 16(a) and 16(b) show the flow structures at frequency ω that are optimal at exciting an energetic response in the flow. These appear to be streamwise-elongated structures near the wall at locations $0 \leqslant x/\theta_0 < 200$ and along the separated shear layer. It supports our hypothesis that the low-frequency motion is most modulated by streamwise-elongated streamwise vortices. Figures 16(c) and 16(d) show the zero-frequency (mean-flow) streamwise velocity component response that can be excited through the harmonic resolvent operator. In particular, we notice that this component has nonzero value at $x/\theta_0 \geqslant 400$, suggesting that an external periodic forcing input should create a nonnegligible net change in momentum downstream of the separation bubble over one forcing period. A favorable net-change in momentum should alleviate the effects of the adverse pressure gradient in the flow, thereby favoring flow reattachment and shrinking of the separation bubble. Indeed, the TSB is observed to be shrunk up to $x/\theta_0 \approx 400$ for actuation at f_l and f_h in the simulations.

IV. CONCLUSIONS

We perform direct numerical simulations of a TSB with streamwise-oriented actuators placed upstream of the mean separation point. The separation over the flat plate is induced by a freestream adverse pressure gradient due to a wall-normal suction on the upper boundary of the domain. The uncontrolled TSB shows a natural low-frequency (f_l) motion besides the high-frequency (f_h) vortex-shedding mode. In the current study, the flow is excited at the natural low (f_l) and high ($f_h = 2.5f_l$) frequencies to examine the response of the TSB. A much higher frequency ($10f_l$) is also tested for comparison. Zero-net-mass-flux actuators that have their long axis oriented in the streamwise direction, an aspect ratio of six, and a width that is the same as the local boundary layer thickness, are employed. They generate counterrotating streamwise vortices during each sinusoidal excitation cycle, which mimic the streamwise-elongated Görtler vortices that have been found to be associated with the low-frequency motion of the uncontrolled TSB. The actuation at f_h and f_l reduces the TSB size by 50% while the $10f_l$ excitation does not affect either the instantaneous or the mean TSB. The early reattachment leads to a higher total friction drag but more pressure recovery.

The results show the separating boundary layer responds strongly to actuation at f_h and f_l. The structures in the separated shear layer change from nests of 3D vortices in the uncontrolled case to 2D roller vortices. The strong coherence of the 2D vortices may cause local flow separation, the formation of secondary vortices, and other turbulent structures related to additional instabilities besides the KH and Görtler instabilities. Unsteadiness of the instantaneous wall shear stress, the

area of the reversed flow region, and the magnitude and anisotropy of velocity fluctuations are much amplified (become many times larger than the time-averaged values) due to the structural changes of the flow. The size of the mean separation bubble is not determined by the turbulent diffusion of momentum by small eddies but by the decay rate of these very-large-scale vortices. A number of mechanisms affect the decay rate such as the dynamics of a counter-rotating vortex pair and interaction between consecutive vortices with the same direction of rotation. The shedding frequency of the very-large-scale vortices agrees with that of the actuation frequency. Low-frequency unsteadiness still exists in all cases regardless of the forcing frequency. Since the Görtler instability was found to be associated with the formation of large-scale vorticity packets in the uncontrolled case, it is possible that the very-large-scale vortices formed at f_h and f_l are due to the amplified Görtler instability triggered by the streamwise-oriented actuators used in this study.

The present study shows that the low-frequency motion can be modulated by small streamwise perturbations thus leading to smaller ($\sim$50%) mean separation region. Note that C_μ employed here is quite small ($C_\mu \sim \mathcal{O}(10^{-4})$), comparable to the ones used to trigger laminar-to-turbulent transition for laminar separation control. However, friction drag is increased while the pressure loss is reduced. For different engineering applications, effectiveness of flow control should be determined based on the performance of interest rather than simply the size of the separated region with flow reversal. It is also necessary to consider the amplification of stress/load unsteadiness as a possibly harmful outcome of the flow control.

The linear harmonic resolvent analysis is performed with a periodic base flow consisting of the mean flow and the low-frequency unsteadiness. The perturbations that excite the most energetic response in the flow for the low-frequency motion are found to be streamwise-elongated structures, supporting our previous finding the breathing mode of this TSB is indeed related to the streamwise-elongated Görter vortices. It also shows that the choice of using streamwise-oriented actuators to produce such vortices in this study is well justified. The most significant response of the mean flow to actuation also agrees with the simulation: the separation bubble is reduced in size by 50%. Since the resolvent analysis shows the preferred response of the mean flow to the forcing occurs at the natural low frequency, we anticipate that the flow will act as a band-pass filter if broadband signals are applied via open-loop actuation. This paper highlights the importance of physics-based flow control design: actuation should be designed based on the understanding of the dominant physics of the target phenomena, including the dynamical mechanism, scales, structures, etc. Moreover, the actuation may generate other unexpected instabilities/interactions whose roles in the control should be further examined. Extensions to other geometries and actuation schemes may well alter the flow physics and the resulting physics-based control design.

It should be emphasized that the response to flow control strongly depends on the flow configuration and actuation type. In other flows that significantly deviates from the current configuration, the dominant mechanism of separation and reattachment may be very different that the observations in this paper are less prominent or even not valid. For instance, when flow separation occurs due to the expansion of the crossflow area (i.e., geometry induced separation), the distance between the roller vortex in the separated shear layer and the wall may increase after the flow detaches. The secondary vortex will not be able to be induced in this case. The absence of the vortex pair interaction may cause the roller vortex to decay slower and lead to a less-reduced mean separation region. Another example is a flow separating at a backward-facing step. There is no convex streamline curvature during separation. Thus, Görtler instability does not play a role in such flow. Using the actuator employed here may not get good response. The present work is limited to a small parameter space. Future work may focus on the strength, spacing and size of the actuator.

Also note that the separation point in this configuration is nearly fixed at $x = 164\theta_o$ by the imposed suction profile. In other configurations where the freestream pressure gradient can be altered by the actuation, e.g., geometry-induced separation in which inviscid-viscous interaction is critical, the response of the separating flow to different frequencies may vary. The results of resolvent analysis is suitable for qualitative comparison only since the actual TSB is highly

nonlinear. The preferred frequency may vary when more unsteady modes are included in the base flow.

ACKNOWLEDGMENTS

[1] M. Gad-el-Hak and D. M. Bushnell, Separation control: Review, J. Fluids Eng. **113**, 5 (1991).

[2] H. E. Monir, M. Tadjfar, and A. Bakhtian, Tangential synthetic jets for separation control, J. Fluids Struct. **45**, 50 (2014).

[3] D. Williams and D. MacMynowski, *Fundamentals and Applications of Modern Flow Control*, edited by R. D. Joslin and D. N. Miller (AIAA, Reston, VA, 2009), pp. 1–20

[4] L. N. Cattafesta and M. Sheplak, Actuators for active flow control, Annu. Rev. Fluid Mech. **43**, 247 (2011).

[5] M. Amitay, D. Smith, V. Kibens, D. E. Parekh, and A. Glezer, Aerodynamic flow control using synthetic jet actuators, AIAA J. **39**, 361 (2001).

[6] S. D. Goodfellow, S. Yarusevych, and P. E. Sullivan, Momentum coefficient as a parameter for aerodynamic flow control with synthetic jets, AIAA J. **51**, 623 (2013).

[7] H. Shan, L. Jiang, and C. Liu, Direct numerical simulation of flow separation around a NACA 0012 airfoil, Comput. Fluids **34**, 1096 (2005).

[8] E. A. Deem, L. N. Cattafesta, M. S. Hemati, H. Zhang, C. Rowley, and R. Mittal, Adaptive separation control of a laminar boundary layer using online dynamic mode decomposition, J. Fluid Mech. **903**, A21 (2020).

[9] J. H. Seo, F. Cadieux, R. Mittal, E. Deem, and L. N. Cattafesta, Effect of synthetic jet modulation schemes on the reduction of a laminar separation bubble, Phys. Rev. Fluids **3**, 033901 (2018).

[10] H. Jiang and L. Cheng, Flow separation around a square cylinder at low to moderate Reynolds numbers, Phys. Fluids **32**, 044103 (2020).

[11] R. L. Simpson, Aspects of turbulent boundary-layer separation, Prog. Aerosp. Sci. **32**, 457 (1996).

[12] J.-C. Béra, M. Michard, M. Sunyach, and G. Comte-Bellot, Changing lift and drag by jet oscillation: Experiments on a circular cylinder with turbulent separation, Eur. J. Mech. B Fluids **19**, 575 (2000).

[13] S. Chun and H. J. Sung, Large-scale vortical structure of turbulent separation bubble affected by unsteady wake, Exp. Fluids **34**, 572 (2003).

[14] D. Pearson, P. Goulart, and B. Ganapathisubramani, Turbulent separation upstream of a forward-facing step, J. Fluid Mech. **724**, 284 (2013).

[15] G. N. Coleman, C. L. Rumsey, and P. R. Spalart, Numerical study of turbulent separation bubbles with varying pressure gradient and Reynolds number, J. Fluid Mech. **847**, 28 (2018).

[16] A. T. Mohammed-Taifour and J. Weiss, Periodic forcing of a large turbulent separation bubble, J. Fluid Mech. **915**, A24 (2021).

[17] M. Sato, K. Asada, T. Nonomura, H. Aono, A. Yakeno, and K. Fujii, Mechanisms for turbulent separation control using plasma actuator at Reynolds number of 1.6×10^6, Phys. Fluids **31**, 095107 (2019).

[18] M. J. Cho, S. Choi, and H. Choi, Control of flow separation in a turbulent boundary layer using time-periodic forcing, J. Fluid Engr. **138**, 101204 (2016).

[19] S. Song and J. K. Eaton, The effects of wall roughness on the separated flow over a smoothly contoured ramp, Exp. Fluids **33**, 38 (2002).

[20] C. D. Aubertine, J. K. Eaton, and S. Song, Parameters controlling roughness effects in a separating boundary layer, Int. J. Heat Fluid Flow **25**, 444 (2004).

[21] W. Wu, R. Banyassady, and U. Piomelli, Large-eddy simulation of impinging jets on smooth and rough surfaces, J. Turbul. **17**, 847 (2016).

[22] W. Wu and U. Piomelli, Effects of surface roughness on a separating turbulent boundary layer, J. Fluid Mech. **841**, 552 (2018).

[23] P.-A. Krogstad and P. E. Skare, Influence of a strong adverse pressure gradient on the turbulent structure in a boundary layer, Phys. Fluids **7**, 2014 (1995).

[24] H. S. Shafi and R. A. Antonia, Anisotropy of the Reynolds stress in a turbulent boundary layer on a rough wall, Exp. Fluids **18**, 213 (1995).

[25] J. Yuan and U. Piomelli, Roughness effects on the Reynolds stress budgets in near-wall turbulence, J. Fluid Mech. **760**, R1 (2014).

[26] W. Wu, U. Piomelli, and J. Yuan, Turbulence statistics in rotating channel flows with rough walls, Int. J. Heat Fluid Flow **80**, 108467 (2019).

[27] A. Seifert, A. Darabi, and I. Wygnanski, Delay of airfoil stall by periodic excitation, J. Aircraft **33**, 691 (1996).

[28] R. Mittal and R. Kotapati, Resonant mode interaction in a canonical separated flow, in *Proceedings of the 6th IUTAM Symposium on Laminar-Turbulent Transitions* (Springer, Berlin, 2006), pp. 341–348.

[29] M. A. Leschziner and S. Lardeau, Simulation of slot and round synthetic jets in the context of boundary-layer separation control, Philos. Trans. R. Soc. A **369**, 1495 (2011).

[30] T. T. Rice, K. Taylor, and M. Amitay, Pulse modulation of synthetic jet actuators for control of separation, Phys. Rev. Fluids **6**, 093902 (2021).

[31] L. W. Sigurdson, The structure and control of a turbulent reattaching flow, J. Fluid Mech. **298**, 139 (1995).

[32] M. Amitay and A. Glezer, Role of actuation frequency in controlled flow reattachment over a stalled airfoil, AIAA J. **40**, 209 (2002).

[33] A. Glezer, M. Amitay, and A. M. Honohan, Aspects of low- and high-frequency aerodynamic flow control, AIAA J. **43**, 1501 (2005).

[34] A. Esfahani, N. Webb, and M. Samimy, Flow separation control over a thin post-stall airfoil: Effects of excitation frequency, AIAA J. **57**, 1826 (2019).

[35] J. Dandois, E. Garnier, and P. Sagaut, Numerical simulation of active separation control by a synthetic jet, J. Fluid Mech. **574**, 25 (2007).

[36] J. A. Franck and T. Colonius, Effects of actuation frequency on flow control applied to a wall-mounted hump, AIAA J. **50**, 1631 (2012).

[37] Y. Na and P. Moin, Direct numerical simulation of a separated turbulent boundary layer, J. Fluid Mech. **374**, 379 (1998).

[38] A. Mohammed-Taifour and J. Weiss, Unsteadiness in a large turbulent separation bubble, J. Fluid Mech. **799**, 383 (2016).

[39] W. Wu, C. Meneveau, and R. Mittal, Spatio-temporal dynamics of turbulent separation bubbles, J. Fluid Mech. **883**, A45 (2019).

[40] R. A. Humble, F. Scarano, and B. W. V. Oudheusden, Unsteady aspects of an incident shock wave/turbulent boundary layer interaction, J. Fluid Mech. **635**, 47 (2009).

[41] A. Thacker, S. Aubrun, A. Leroy, and P. Devinant, Experimental characterization of flow unsteadiness in the centerline plane of an Ahmed body rear slant, Exp. Fluids **54**, 1479 (2013).

[42] N. Gautier, J. L. Aider, T. Duriez, B. R. Noack, M. Segond, and M. W. Abel, Closed-loop separation control using machine learning, J. Fluid Mech. **770**, 442 (2015).

[43] A. Debien, S. Aubrun, N. Mazellier, and A. Kourta, Active separation control process over a sharp edge ramp, in *Proceedings of the 9th International Symposium on Turbulence and Shear Flow Phenomena (TSFP 9)* (Melbourne, Australia, 2015), pp. 311–322.

[44] A. Debien, K. A. F. F. von Krbek, N. Mazellier, T. Duriez, L. Cordier, B. R. Noack, M. W. Abel, and A. Kourta, Closed-loop separation control over a sharp edge ramp using genetic programming, Exp. Fluids **57**, 40 (2016).

[45] F. H. Clauser, Turbulent boundary layers in adverse pressure gradient, J. Aeronaut. Sci. **21**, 91 (1954).

[46] T. Lund, X. Wu, and K. Squires, Generation of turbulent inflow data for spatially developing boundary layer simulations, J. Comput. Phys. **140**, 233 (1998).

[47] I. Orlanski, A simple boundary condition for unbounded hyperbolic flows, J. Comput. Phys. **21**, 251 (1976).

[48] G. S. Settles, T. J. Fitzpatrick, and S. M. Bogdonoff, Detailed study of attached and separated compression corner flowfields in high Reynolds number supersonic flow, AIAA J. **17**, 579 (1979).

[49] M. S. Loginov, N. A. Adams, and A. A. Zheltovodov, Large-eddy simulation of shock-wave/turbulent-boundary-layer interaction, J. Fluid Mech. **565**, 135 (2006).

[50] S. Priebe, J. H. Tu, C. W. Rowley, and M. P. Martín, Low-frequency dynamics in a shock-induced separated flow, J. Fluid Mech. **807**, 441 (2016).

[51] R. Petz and W. Nitsche, Active separation control on the flap of a two-dimensional generic high-lift configuration, J. Aircraft **44**, 865 (2007).

[52] J. Dandois, E. Garnier, and P. Sagaut, Unsteady simulation of a synthetic jet in a crossflow, AIAA J. **44**, 225 (2006).

[53] D. K. L. Wu and M. A. Leschziner, Large-eddy simulations of circular synthetic jets in quiescent surroundings and in turbulent cross-flow, Int. J. Heat Fluid Flow **30**, 421 (2009).

[54] D. R. Smith, Interaction of a synthetic jet with a crossflow boundary layer, AIAA J. **40**, 2277 (2002).

[55] T. V. Buren, C. M. Leong, E. Whalen, and M. Amitay, Impact of orifice orientation on a finite-span synthetic jet interaction with a crossflow, Phys. Fluids **28**, 037106 (2016).

[56] S. Aram and R. Mittal, Computational study of the effect of slot orientation on synthetic jet-based separation control, Int. J. Flow Control **3**, 87 (2011).

[57] R. Raju, R. Mittal, and L. Cattafesta, Dynamics of airfoil separation control using zero-net mass-flux forcing, AIAA J. **46**, 3103 (2008).

[58] W. Wu, J.-H. Seo, C. Meneveau, and R. Mittal, Response of a laminar separation bubble to forcing with zero-net mass flux jets, in *Proceedings of the Flow Control Conference*, AIAA AVIATION Forum (AIAA, 2018).

[59] R. J. Goldstein, Flim cooling, Adv. Heat Transfer **7**, 321 (1971).

[60] T. V. Buren, E. Whalen, and M. Amitay, Interaction between a vortex generator and a synthetic jet in a crossflow, Phys. Fluids **27**, 107101 (2015).

[61] H. Abe, Reynolds-number dependence of wall-pressure fluctuations in a pressure-induced turbulent separation bubble, J. Fluid Mech. **833**, 563 (2017).

[62] L. G. Pack, N. W. Schaeffler, C.-S. Yao, and A. Seifert, Active control of flow separation from the slat shoulder of a supercritical airfoil, in *AIAA Paper* (AIAA AVIATION Forum, 2002), pp. 2002–3156.

[63] W. Wu, C. Meneveau, and R. Mittal, Dynamics of natural and perturbed turbulent separation bubbles, in *Proceedings of the 11th International Symposium on Turbulence and Shear Flow Phenomena (TSFP 11)* (Southampton, UK, 2019).

[64] R. Mittal, H. Dong, M. Bozkurttas, F. Najjar, A. Vargas, and A. von Loebbecke, A versatile sharp interface immersed boundary method for incompressible flows with complex boundaries, J. Comput. Phys. **227**, 4825 (2008).

[65] W. Wu, J. Seo, C. Meneveau, and R. Mittal, Response of a laminar separation bubble to forcing with zero-net mass flux jets, in *Proceedings of the Flow Control Conference*, AIAA AVIATION Forum (AIAA, 2018).

[66] D. R. Smith, M. Amitay, K. Kibens, D. E. Parekh, and A. Glezer, Modification of lifting body aerodynamics using synthetic jet actuators, in *AIAA Paper* (AIAA AVIATION Forum, 1998).

[67] D. Greenblatt and I. J. Wygnanski, The control of flow separation by periodic excitation, Prog. Aerosp. Sci. **36**, 487 (2000).

[68] T. E. Lee, J. G. Leishman, and M. Ramasamy, Fluid dynamics of interacting blade tip vortices with a ground plane, J. Am. Helicopter Soc. **55**, 22005 (2010).

[69] J. Geiser and K. T. Kiger, Vortex ring breakdown induced by topographic forcing, J. Phys.: Conf. Ser. **318**, 062013 (2011).

[70] W. Wu and U. Piomelli, Large-eddy simulation of impinging jets with embedded azimuthal vortices, J. Turbul. **16**, 44 (2015).

[71] J. Otsuka, A. Saruwatari, and Y. Watanabe, Vortex-induced suspension of sediment in the surf zone, Adv. Water Resour. **110**, 59 (2017).

[72] D. Liepmann and M. Gharib, The role of streamwise vorticity in the near field entrainment of round jets, J. Fluid Mech. **245**, 643 (1992).

[73] R. Suprayan and H. E. Fiedler, On streamwise vortical structures in the near-field of axisymmetric shear layers, Meccanica **29**, 403 (1994).

[74] P. E. Skare and P.-A. Krogstad, A turbulent equilibrium boundary layer near separation, J. Fluid Mech. **272**, 319 (1994).

[75] A. Padovan, S. E. Otto, and C. W. Rowley, Analysis of amplification mechanisms and cross-frequency interactions in nonlinear flows via the harmonic resolvent, J. Fluid Mech. **900**, A14 (2020).

[76] M. R. Jovanović and B. Bamieh, Componentwise energy amplification in channel flows, J. Fluid Mech. **534**, 145 (2005).

[77] B. J. McKeon and A. S. Sharma, A critical-layer framework for turbulent pipe flow, J. Fluid Mech. **658**, 336 (2010).

[78] N. Halko, P. G. Martinsson, and J. A. Tropp, Finding structure with randomness: Probabilistic algorithms for constructing approximate matrix decompositions, SIAM Rev. **53**, 217 (2011).